Experimental Mechanics (2014) 54:1673–1685
DOI 10.1007/s11340-014-9953-4

A novel ultrasonic strain gauge for single-sided measurement of a local 3D strain field

Mathias Kersemans · Klaas Allaer · Wim Van Paepegem · Koen Van Den Abeele · Lincy Pyl · Filip Zastavnik · Hugo Sol · Joris Degrieck

Received: 28 April 2014 / Accepted: 10 September 2014 / Published online: 19 September 2014

Abstract A novel method is introduced for the measurement of a 3D strain field by exploiting the interaction between ultrasound waves and geometrical characteristics of the insonified specimen. First, the response of obliquely incident harmonic waves to a deterministic surface roughness is utilized. Analysis of backscattered amplitudes in Bragg diffraction geometry then yields a measure for the in-plane strain field by mapping any shift in angular dependency. Secondly, the analysis of the reflection characteristics of normal incident pulsed waves in frequency domain provides a measure of the out-of-plane normal strain field component, simply by tracking any change in the stimulation condition for a thickness resonance. As such, the developed ultrasonic strain gauge yields an absolute, contactless and single-sided mapping of a local 3D strain field, in which both sample preparation and alignment procedure are needless. Results are presented for cold-rolled DC06 steel samples onto which skin passing of the work rolls is applied. The samples have been mechanically loaded, introducing plastic strain levels ranging from 2 % up to 35 %. The ultrasonically measured strains have been validated with various other strain measurement techniques, including manual micrometer, longitudinal and transverse mechanical extensometer and optical mono- and stereovision digital image correlation. Good agreement has been obtained between the ultrasonically determined strain values and the results of the conventional methods. As the ultrasonic strain gauge provides all three normal strain field components, it has been employed for the extraction of Lankford ratios at different applied longitudinal plastic strain levels, revealing a strain dependent plastic anisotropy of the investigated DC06 steel sheet.

Keywords Ultrasound · Local 3D strain measurement · DC06 steel · Lankford ratio

M. Kersemans (✉) · K. Allaer · W. Van Paepegem · J. Degrieck
Department of Materials Science and Engineering, Ghent University, Technologiepark-Zwijnaarde 903, 9052 Zwijnaarde, Belgium
e-mail: Mathias.Kersemans@UGent.be

M. Kersemans
e-mail: MathiasKersemans@hotmail.com

K. Van Den Abeele
Department of Physics, Catholic University of Leuven - KULAK, Etienne-Sabbelaan 52, 8500 Kortrijk, Belgium

L. Pyl · F. Zastavnik · H. Sol
Department Mechanics of Materials and Constructions, Vrije Universiteit Brussel, Pleinlaan 2, 1050 Brussels, Belgium

Introduction

Measurement of strain evolution is indispensible to understand the response of materials under external loads, as well as to ensure the safety and integrity of a structure during its life time. The strain phenomenon can be subdivided in two main regimes: the elastic and the plastic region. While the reversible elastic region is typically characterized by small strain levels, the irreversible plastic region involves large strains up to tens of percent. On a laboratory scale, the elastic region is of great importance for materials characterization. Most (metallic) industrial structures on the other hand can be subject to extreme or accidental loading conditions during their life time, inducing plastic deformation. Long-distance (off-shore) pipelines for example are exposed to high internal pressure in combination with bending and tension, resulting in large plastic strains [1, 2]. Apart from operationally induced plastic strains, offshore pipelines are already plastically deformed during their installation with a layship, because of reeling strains (before the pipe is released), strains during the release (overbend in S-lay) and strains at the area of laying (sagbend in S-lay) [3]. Buried pipelines on the other hand are exposed to

both temporary (earthquake) and permanent (soil liquefaction) geological settings. For pipelines with, respectively without a girth weld, global plastic strain values up to 5 %, respectively 7.5 % are acceptable. Exceeding the safety limit for plastic deformation could result in failure and rupture of the pipeline.

At present, several different gauging techniques have been developed, including electrical, optical and mechanical methods, for inspecting and monitoring the strain of an engineering structure in order to assure its mechanical health [4–10]. However, most of the existing strain measurement techniques have several drawbacks for use in an industrial environment, including (i) the need for a reference measurement, (ii) the inability to provide strain history, (iii) the necessity to physically attach the gauge, (iv) the limited range of measurable strain fields, (v) the inapplicability for offshore applications and (vi) the large sensitivity to small misalignments and external vibration. Because of the above mentioned factors, pipelines are inspected by inserting a robot provided with a GPS tracking system. Comparison of the original position of the pipeline to its current position, then provides a coarse measure for the global plastic strain. However, it is clear that on the local level, much higher strains are involved which could jeopardize the designed functionality of the pipeline. Hence, there is a need for an innovative means to locally measure a strain field in difficult environmental circumstances.

Recently, it has been shown by the present authors that the in-plane parameters of a periodic (sub)surface structure, i.e. periodicities and symmetry orientations, can be ultrasonically characterized in the Bragg scattering regime [11], simply by evaluating the backscattered wave amplitude for a wide range of oblique incidence angles $\psi(\varphi,\theta)$ [12]. A schematic of the so-called harmonic ultrasonic backscatter polar scan (H-UBPS) method is shown in Fig. 1(a), in which the ultrasonic transducer is operated as both emitter and receiver. A H-UBPS experiment, recorded at f=5 MHz, is displayed in Fig. 1(b) for a polycarbonate plate in which a perfect 2D surface corrugation with a depth of 17 μm is ablated by means of a high-quality excimer laser [12]. The angular axis represents the in-plane orientation angle, further called the polar angle φ, the radial axis the angle with the vertical normal, further called the incident angle θ, while the assigned color pigment is a measure for the backscattered amplitude. Both the periodicities and symmetries of the 2D surface structure are encoded in the exact location of the backscatter spots in the H-UBPS experiment [12].

In this paper, we propose an ultrasonic strain gauge which is partly based on the detection of shifting diffraction peaks in a H-UBPS image. This positional shifting is linked to a transformation of the surface parameters of the inspected material spot, and thus provides a measure for the in-plane strain field. Instead of manufacturing a specific surface corrugation which introduces residual stress concentrations and thus effectively weakens the material, we directly employ the surface roughness left during the manufacturing process. By combining the H-UBPS methodology with the analysis of the reflected ultrasonic broadband pulse at normal incidence in frequency domain, a measurement of the out-of-plane strain field is obtained as well. As such, the here presented technique provides a non-contact and single-sided measurement of the local strain field (the in-plane components as well as the normal out-of-plane component) without the necessity of sample preparation. As the direction of the sample's normal is directly captured in the H-UBPS image, alignment is of minor concern. The ultrasonic strain gauge (USG) technique is demonstrated for the widespread cold-rolled DC06 deep drawing steel, at different levels of plastic strain. The USG measurements are supported and verified by conventional strain measurement techniques, including (i) manual micrometer (MM), (ii) longitudinal and transverse mechanical extensometers (ME), and (iii) both mono- and stereovision digital image correlation (2D- and 3D-DIC).

In the next section, a short description of the DC06 steel material and its loading procedure is introduced. Section III provides a physical background for the working principle of the ultrasonic strain gauge. The results of the different strain gauge techniques are discussed in section IV. At last several conclusions from this study are rephrased in section V.

Materials and experimental procedure

Cold-rolled DC06 steel is considered in this study, having a thickness of d=0.7819±0.0026 mm, a Young's modulus E=189.86±0.59 GPa, a Poisson's ratio ν=0.345±0.001 and a density ρ=7704.7 kg/m^3 [13]. Its chemical composition is summarized by: Carbon C=0.02 % (max), Manganese Mn=0.25 % (max), Phosporus P=0.02 % (max), Sulfur S=0.02 % (max), Silicium Si=0.02 % (max) and Aluminum Al=0.01 % (min) [14]. Like many materials, the DC06 steel is provided by a deterministic surface roughness which has been applied through skin passing of the work rolls in order to meet a designed functionality. In this case (i) to improve the paint bonding capability, (ii) to reduce the waviness after coating and (iii) to lower the friction in a forming process [15]. A microscopic image of the DC06 steel surface texture is shown in Fig. 2(a).

Due to the low surface finishing quality (skin passing), the surface structure is difficult to identify by standard optical microscopy. Therefore, an investigation is performed by means of 3D optical interferometry. An area of 3.6×3.6 mm^2, with spatial sampling of ~3.6 μm in both directions, has been investigated by coherence correlation interferometry (CCI). The vertical range is 100 μm with a depth resolution of 0.01 nm. The processed and filtered image is shown in Fig. 2(b). Following the EN10049 standard (with 0.8 mm

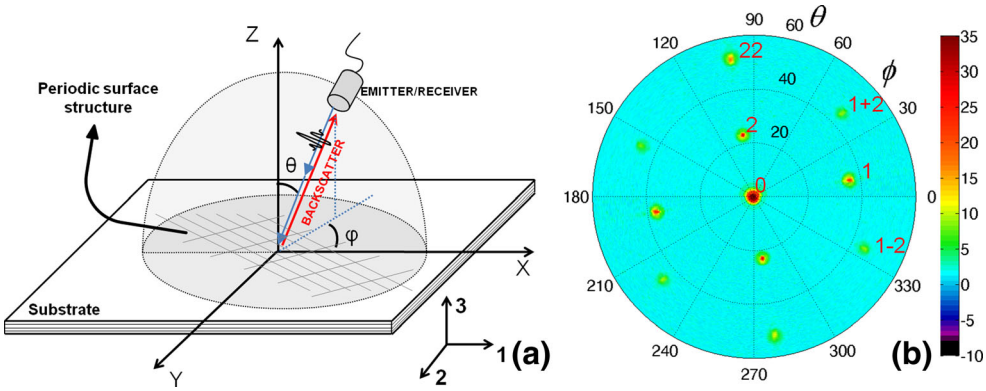

Fig. 1 Schematic of the H-UBPS method (**a**) and H-UBPS recording (f=5 MHz) for a 2D corrugated polycarbonate sample (**b**)

Gauss filter cut-off), an average roughness Ra=1.1 μm with standard deviation σ_{Ra}=0.0502 μm has been determined. From the average power spectrum density, several dominating wave lengths in the surface texture have been extracted: Λ_1 = 243±20.2 μm, Λ_{1+2} = 191±16.0 μm and Λ_2 = 243±23.6 μm with orientation Φ_1 = 53°, Φ_{1+2} = 90° and Φ_2 = 125° respectively. With the present CCI setup, we were not able to further increase the resolution in spatial frequency domain in order to narrow the error bars.

Tensile tests on DC06 sheet material coupons are conducted in accordance to the ASTM E8-08 standard [16]. All experimental tests are performed at room temperature on a 50 kN servo-hydraulic INSTRON 8801 testing machine and are displacement-controlled with a crosshead speed of 2 mm/min. Plastic strains ranging from 2 % up to 35 % are considered (the manufacturer guarantees a minimum elongation of 38 % in the skin passed condition [14]). The induced strains are measured by different strain gauge techniques: (i) manual micrometer (MM), (ii) longitudinal and transverse mechanical extensometers (ME), (iii) mono- and stereovision Digital Image Correlation (2D and 3D DIC) and (iv) the newly developed ultrasonic method (USG). Figure 3a shows the tensile test setup with the extensometers mounted.

Alternatively to the use of extensometers, full field strain maps can be obtained by DIC [17]. This method is based on tracking the geometrical changes in the grey-scale distribution of a speckle pattern which is attached to the specimen surface (see Fig. 3(b-c)). A deformed image is taken at incremental loading steps and compared to the reference image taken prior to loading. This reference image is mapped by a square correlation subset window which is defined by the subset size and step size, being the pixel dimension of one single subset, and the centre distance between two adjacent subset windows, respectively. A correlation algorithm computes the displacement of each subset centre on the deformed image, estimating the displacement field across the region of interest (ROI). Determination the specimen's surface displacement field and subsequent calculation of the strain contours was done using the MatchID software [18]. By calibrating the camera system, intrinsic and extrinsic parameters are taken into account during the image correlation process, ensuring accurate strain results. A random speckle pattern was applied on the

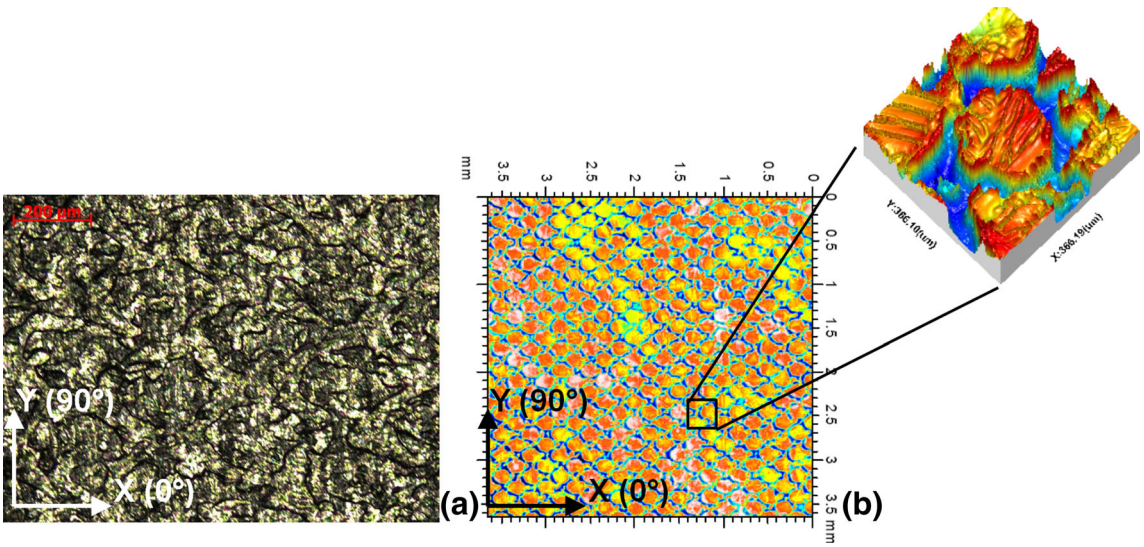

Fig. 2 Optical visualization of the surface structure of DC06 steel: standard 2D microscopy (**a**) and 3D coherence correlation interferometry (after processing) (**b**)

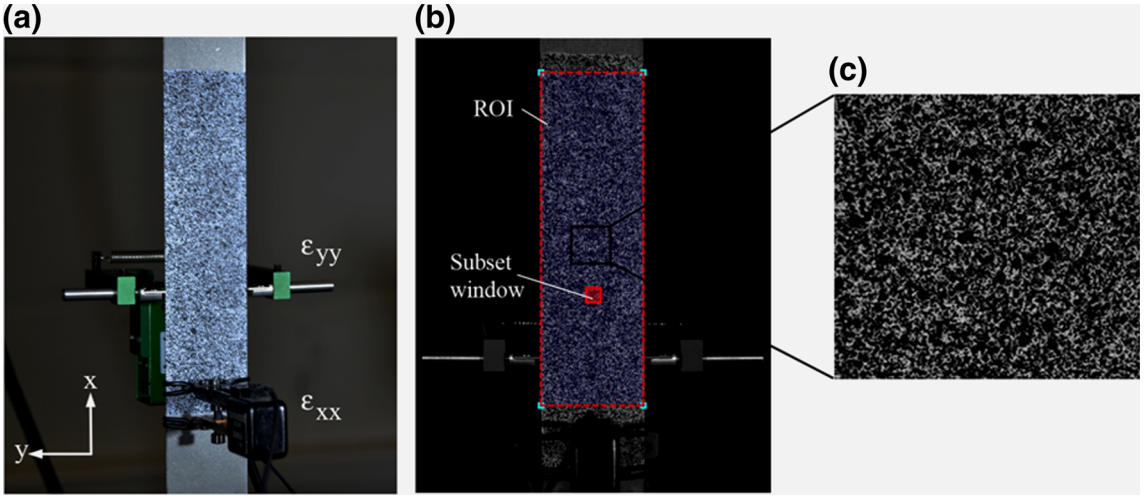

Fig. 3 Experimental setup: longitudinal and transverse mechanical extensometers (**a**), image correlation window with subset size (**b**) and detail of the spray-paint speckle-pattern (**c**)

specimens' surface by aerosol spray-paint and is monitored with 2 mega-pixel 8-bit CCD AVT Stingray F-201 B 1/1.8″ cameras throughout the loading event. During quasi-static loading, images with a 1624×1232 pixel resolution are acquired at a sampling rate of 1 Hz and are synchronized with the load–displacement signals from the tensile machine. Both mono- and stereovision DIC is used to measure the surface displacement fields. In a monovision setup the specimen has to be positioned parallel to the camera sensor plane, and must undergo ideal planar deformation without any out-of-plane displacement. However, in practice out-of-plane motion is likely to occur, introducing an apparent strain [19]. The latter is taken care of by using a stereovision setup.

The ultrasonic measurements have been obtained with an in-house developed automated 5-axis scanner [20] which is provided with a standard piezoelectric transducer (diameter D=13 mm and frequency f=5 MHz) operating as both emitter and receiver. Both quasi-harmonic and pulsed signals can be generated by a programmable signal generator (Tektronix). For the former, only a single period (in the middle of the generated wave train) is considered in the analysis to avoid transient effects [21]. As the current ultrasonic setup is immobile, the samples are first demounted from the tensile machine before scanning in the H-UBPS setup. This is the main reason why only plastic strain fields are considered in this study.

Ultrasonic strain gauge: physical background

In-plane strain field

Insonification of a periodic surface structure according to the H-UBPS methodology yields several well-defined high-amplitude symmetrically positioned backscatter peaks. Basically, the surface structure acts as a diffraction grating for incident ultrasound waves. This has been demonstrated recently for samples provided with a perfect 2D (sub)surface corrugation [12]. An example of a H-UBPS image is given in Fig. 1(b) for a polycarbonate plate provided with an ablated 2D surface structure which can be conceived as two overlapping 1D gratings, grating 1 and grating 2. Spike 0 corresponds to the specular reflection at normal incidence, its position in (φ,θ)-space can be used to compensate for angular misalignment during the experimental recording. The other spikes in the H-UBPS image represent diffraction peaks. Note that the amplitude scale has been cut-off such that saturation occurs for the middle spike 0, whereby the visibility of the various diffraction peaks increases. Spikes 1 and 2 correspond to 1st order diffraction peaks associated to the two overlapping 1D gratings. Spikes 22 correspond to 2th order diffraction peaks associated to the grating 2. The polar angles φ of these diffraction peaks yield the symmetry orientations Φ of the 1D grating according to

$$\Phi = \varphi - 90 \tag{1}$$

The periodicities Λ on the other hand are encrypted in the incident angle θ of these diffraction peaks according to the Bragg relationship for backscatter geometry [11]

$$\Lambda = \frac{m\lambda}{2\sin\theta} \tag{2}$$

with m the diffraction order (integer) and λ the ultrasonic wave length in water. The necessary condition for the presence of backscatter in the Bragg regime is formulated by $\lambda < 2\Lambda$.

Hence, the H-UBPS methodology provides a measure for the characteristic surface parameters $\{\Lambda_1^V, \Phi_1^V, \Lambda_2^V, \Phi_2^V\}$, where

the superscript 'V' denotes the virgin state (or unstrained state) of the insonified specimen, the subscript refers to the corresponding 1D grating. Spikes (1+2), respectively spikes (1–2) are joint-diffraction spikes associated to both the 1D gratings, and are understood by considering the addition, respectively subtraction, of the reciprocal grating parameters. These joint-diffraction spikes can serve as an additional check for the accuracy of the determined corrugation parameters [12].

When subjected to an external load, the structure gets strained and in extension the parameters of the deterministic surface roughness transform. As such, the peaks in the H-UBPS scan of the strained sample shift position with respect to the results of the unstrained sample. Hence, analyzing the H-UBPS image for a strained sample, an updated set of surface parameters $\{\Lambda_1^S,\Phi_1^S,\Lambda_2^S,\Phi_2^S\}$ can be extracted (the superscript 'S' denoted the strained state). Knowledge of the in-plane surface parameters $\{\Lambda_1,\Phi_1,\Lambda_2,\Phi_2\}$ of both the virgin and the strained sample is in principle sufficient to extract the applied in-plane strain field. A schematic of the geometry of a typical surface unit cell is displayed in Fig. 4 for a sample in the virgin state and in the strained state. The coordinate system can be chosen in an arbitrary way. Then, by fixing the extracted surface parameters $\{\Lambda_1,\Phi_1,\Lambda_2,\Phi_2\}$ and constructing their normals, a quadrangle with vertices $\{A,B,C,D\}$ and $\{A',B',C',D'\}$ for the virgin, respectively strained case is obtained.

The coordinates of the vertices can be written in terms of the ultrasonically extracted surface parameters for the virgin and strained sample

$$\begin{cases} A(x,y) = (0,0) \\ B(x,y) = \left(\dfrac{\Lambda_1^V}{\cos\left(\Phi_2^V - 90 - \Phi_1^V\right)} \cos\left(\Phi_2^V - 90\right), \dfrac{\Lambda_1^V}{\cos\left(\Phi_2^V - 90 - \Phi_1^V\right)} \sin\left(\Phi_2^V - 90\right) \right) \\ C(x,y) = \left(\dfrac{\Lambda_1^V}{\cos\left(\Phi_1^V\right)}, 0 \right) = \left(\dfrac{\Lambda_2^V}{\cos\left(\Phi_2^V\right)}, 0 \right) \\ D(x,y) = \left(\dfrac{\Lambda_2^V}{\cos\left(\Phi_1^V - 90 - \Phi_2^V\right)} \cos\left(\Phi_1^V - 90\right), \dfrac{\Lambda_2^V}{\cos\left(\Phi_1^V - 90 - \Phi_2^V\right)} \sin\left(\Phi_1^V - 90\right) \right) \\ O(x,y) = \left(\dfrac{\Lambda_1^V}{2\cos\left(\Phi_1^V\right)}, 0 \right) \end{cases} \tag{3}$$

respectively

$$\begin{cases} A'(x',y') = (0,0) \\ B'(x',y') = \left(\dfrac{\Lambda_1^S}{\cos\left(\Phi_2^S - 90 - \Phi_1^S\right)} \cos\left(\Phi_2^S - 90\right), \dfrac{\Lambda_1^S}{\cos\left(\Phi_2^S - 90 - \Phi_1^S\right)} \sin\left(\Phi_2^S - 90\right) \right) \\ C'(x',y') = \left(\begin{array}{c} \dfrac{\Lambda_1^S}{\cos\left(\Phi_2^S - 90 - \Phi_1^S\right)} \cos\left(\Phi_2^S - 90\right) + \dfrac{\Lambda_2^S}{\cos\left(\Phi_1^S - 90 - \Phi_2^S\right)} \cos\left(\Phi_1^S - 90\right), \\ \dfrac{\Lambda_1^S}{\cos\left(\Phi_2^S - 90 - \Phi_1^S\right)} \sin\left(\Phi_2^S - 90\right) + \dfrac{\Lambda_2^S}{\cos\left(\Phi_1^S - 90 - \Phi_2^S\right)} \sin\left(\Phi_1^S - 90\right) \end{array} \right) \\ D'(x',y') = \left(\dfrac{\Lambda_2^S}{\cos\left(\Phi_1^S - 90 - \Phi_2^S\right)} \cos\left(\Phi_1^S - 90\right), \dfrac{\Lambda_2^S}{\cos\left(\Phi_1^S - 90 - \Phi_2^S\right)} \sin\left(\Phi_1^S - 90\right) \right) \\ O'(x',y') = \left(\begin{array}{c} \dfrac{\Lambda_1^S}{2\cos\left(\Phi_2^S - 90 - \Phi_1^S\right)} \cos\left(\Phi_2^S - 90\right) + \dfrac{\Lambda_2^S}{2\cos\left(\Phi_1^S - 90 - \Phi_2^S\right)} \cos\left(\Phi_1^S - 90\right), \\ \dfrac{\Lambda_1^S}{2\cos\left(\Phi_2^S - 90 - \Phi_1^S\right)} \sin\left(\Phi_2^S - 90\right) + \dfrac{\Lambda_2^S}{2\cos\left(\Phi_1^S - 90 - \Phi_2^S\right)} \sin\left(\Phi_1^S - 90\right) \end{array} \right) \end{cases} \tag{4}$$

Evaluation of the translation and rotation of the vertices then provides a measure for the local strain field. Assuming a linear approximation, the engineering strain field components are obtained

$$\begin{cases} \varepsilon_{xx} = \dfrac{\left\| \overrightarrow{A_x C_x} \right\| - \left\| \overrightarrow{A_x' C_x'} \right\|}{\left\| \overrightarrow{A_x C_x} \right\|} \\ \varepsilon_{yy} = \dfrac{\left\| \overrightarrow{B_y D_y} \right\| - \left\| \overrightarrow{B_y' D_y'} \right\|}{\left\| \overrightarrow{B_y D_y} \right\|} \\ \gamma_{xy} = \cos^{-1}\left(\dfrac{\overrightarrow{AO} \cdot \overrightarrow{OB}}{\left\| \overrightarrow{AO} \right\| \left\| \overrightarrow{OB} \right\|} \right) - \cos^{-1}\left(\dfrac{\overrightarrow{AO} \cdot \overrightarrow{OB}}{\left\| \overrightarrow{AO} \right\| \left\| \overrightarrow{OB} \right\|} \right) \end{cases} \tag{5}$$

By means of equations (3), (4) and (5), the three in-plane engineering strain components can then be explicitly written as a function of the ultrasonically determined surface parameters. As the obtained strain components are determined in the coordinate system of the scanner with basis $\left(\overrightarrow{e_x}, \overrightarrow{e_y}\right)$, a transformation is applied in order to obtain the engineering strain components in the material coordinate system $\left(\overrightarrow{e_{x*}}, \overrightarrow{e_{y*}}\right)$:

$$\begin{bmatrix} \varepsilon_{xx}^* & \varepsilon_{xy}^* \\ \varepsilon_{xy}^* & \varepsilon_{yy}^* \end{bmatrix} = \overline{\overline{R}} \begin{bmatrix} \varepsilon_{xx} & \varepsilon_{xy} \\ \varepsilon_{xy} & \varepsilon_{yy} \end{bmatrix} \overline{\overline{R}}^T \tag{6}$$

with $\overline{\overline{R}}$ the rotation tensor and the superscript T the transpose operator.

The rotation tensor $\overline{\overline{R}}$ is defined as

$$\overline{\overline{R}} = \begin{bmatrix} e_{x*} \cdot e_x & e_{x*} \cdot e_y \\ e_{y*} \cdot e_x & e_{y*} \cdot e_y \end{bmatrix} \tag{7}$$

The principal directions are then easily found by setting $\varepsilon_{xy}^*=0$, for which the following equation is obtained in case of plane strain:

$$\tan(2\alpha) = \frac{2\varepsilon_{xy}}{\varepsilon_{xx} - \varepsilon_{yy}} \tag{8}$$

Solving for α and substituting in equation (6) then yields the principal in-plane strain components at the surface.

It is clear that the imposed strain field could transform the surface parameters such that the inequality $\lambda<2\Lambda$ is not satisfied anymore. Therefore, the bounds for the operational frequency of the ultrasonic wave should be chosen narrower. Considering a maximum strain of ε, the inequality becomes $\lambda<2(1-\varepsilon)\Lambda$ and thus imposes no real limitation to the here described technique.

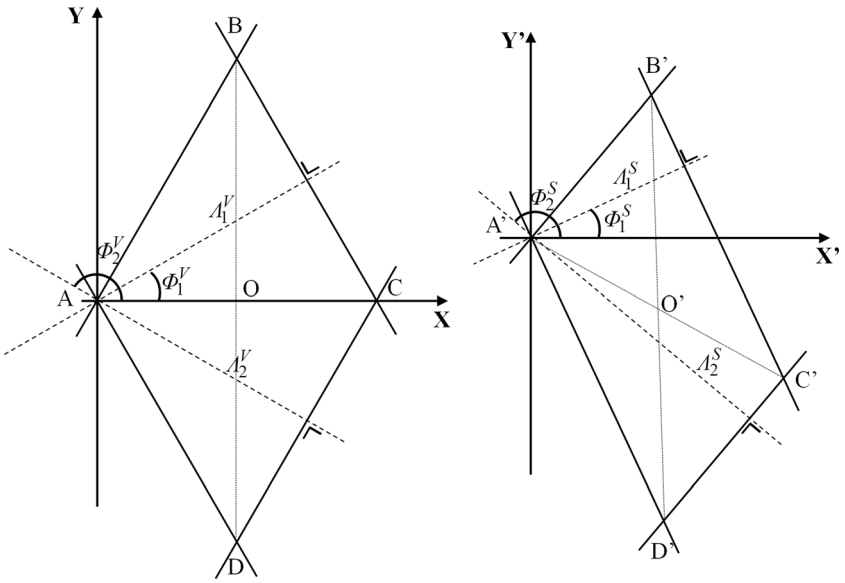

Fig. 4 Schematic of the surface parameters of a virgin (superscript V) (**a**) and a strained (superscript S) (**b**) sample

Out-of-plane strain field

As we investigate in-plane plastic strain fields up to 35 %, it is clear that also the out-of-plane deformation will play an important role. However, with the above described procedure it is not possible to extract the out-of-plane normal strain component ε_{zz}. By insonifying the sample at normal incidence and simply evaluating changes in the difference of the time-of-flight (TOF) values between the ultrasonic echoes from top and bottom interface, one could get a measure for the thickness. Such a thickness measurement technique is already well adopted in industry, despite its lack of accuracy when small thickness variations due to loading conditions are measured. More importantly, often thin sections have to be inspected (as in the present case), which causes overlapping of the top and bottom echo making the unambiguous determination of the TOF values difficult, if not impossible. For these reasons, we exploit the phenomenon of thickness resonances for the extraction of thickness information, and in extension the out-of-plane normal strain component. Figure 5(a) displays the dispersion curves *θ(fd)*, prescribing the conditions for efficient stimulation of Lamb waves under plane-wave insonification, for an immersed DC06 steel plate. The dispersion curves have been computed on the basis of a Legendre polynomial expansion [22], while the DC06 steel is modeled as a viscoelastic solid. The real valued elastic parameters were already given above, the imaginary valued attenuation parameters are a fraction 0.5 % of the elastic parameters.

At normal incidence, i.e. $\theta=0°$, several frequency-thickness values *fd* (indicated with arrows in Fig. 5(a)) give rise to the stimulation of a thickness resonance, causing a dip in the reflection and a peak in the transmission characteristic (see Fig. 5(b)). This resonance phenomenon can be roughly considered as the ultrasonic analogue of the well-known Fabry-Perot optical interferometer. Hence, by evaluating the spectral frequency response of a specularly reflected (or transmitted) broadband pulse at normal incidence, one can track down these dips (or peaks). Since neither the viscoelastic properties of the investigated sample, nor the frequency of the emitting transducer change upon straining, any positional shift of the dip (or peak) in *fd*-space is thus linearly related to a variation in thickness *d* and in extension to the normal out-of-plane engineering strain component ε_{zz}:

$$\varepsilon_{zz} = \frac{d^S - d^V}{d^V} \tag{9}$$

Results and discussion

As an example, we present and discuss the results obtained for the DC06-10 sample which has been subjected to a plastic strain field of more or less 30 % (Fig. 6(a)).

The most rudimentary strain measurement comprises the use of a micrometer. By measuring the width and thickness of both the virgin and the strained sample, the engineering strain in both *y*- and *z*-direction can be extracted. Because of obvious reasons, the measurement of the strain component in *x*-direction cannot be done. The MM measurements have been obtained at three different physical zones L_1, L_2 and L_3 (see Fig. 6(c)) in order to track down lateral non-uniformity of the induced plastic strain field. To lower the error on the MM measurements, each time ten sets of measurements have been performed from which an average value and a measure for the standard deviation is obtained. The MM results for the three spots of DC06-10 are listed in Table 1 (row MM). It can be

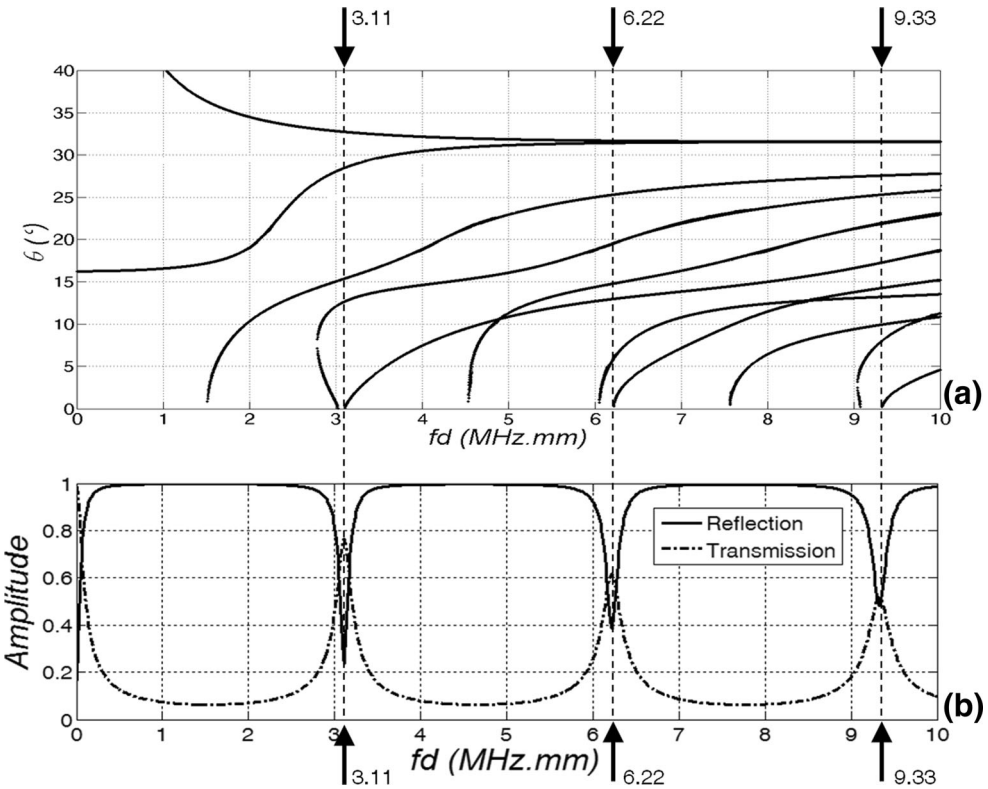

Fig. 5 Dispersion curves *θ(fd)* (**a**) and reflection/transmission characteristics at $\theta=0°$ (**b**) for water-immersed DC06 steel. The thickness resonances are indicated by the arrows

observed that the obtained results suggest a small degree of non-uniformity for the strain field of the DC06-10 sample.

Secondly, the strain during loading of the specimen was also measured with mechanical extensometers, both in longitudinal and in transverse direction. Transverse strain measurements could only be captured at lower strain amplitudes, this because the travel of the transverse extensometer is limited to ± 2.5 mm. The results of the extensometer measurements are added to Table 1 (row ME). The ME results have been put in gray as they have been obtained at one fixed location which furthermore differs from L_1, L_2 and L_3 in order to avoid overlap with the DIC speckle pattern (see Fig. 3(a)). As such, comparison with results obtained at locations L_1, L_2 and L_3 should be done with caution considering the non-uniformity of the strain field. Furthermore, the ME signal in the transverse direction saturated, making the measurement in *y*-direction useless.

To support previous results, we performed both mono- and stereovision digital image correlation. For both methods a correlation subset window of 31 pixels was used, with a step size of 5 pixels. The reference subset is mapped to the deformed subset using an affine transformation function relating the coordinates of the undeformed image to the coordinates of the deformed image. Cross-correlation between reference and

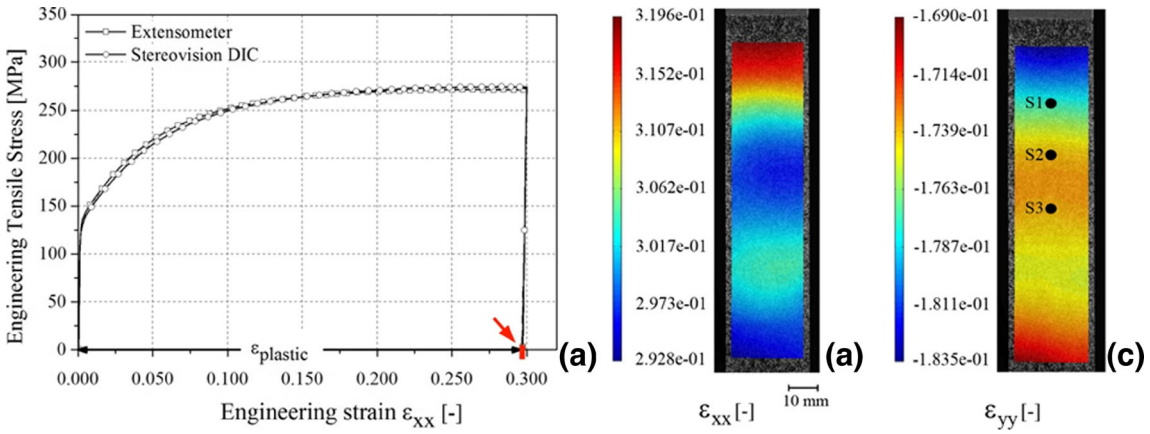

Fig. 6 Tensile stress–strain response of sample DC06-010 (**a**), stereovision DIC extracted contours of the longitudinal (**b**) and transverse (**c**) strain component

Table 1 Strain field measurements (average values ± standard deviation) for the three different spots of sample DC06-10

	Location L_1			Location L_2			Location L_3		
	ε_{xx} (%)	ε_{yy} (%)	ε_{zz} (%)	ε_{xx} (%)	ε_{yy} (%)	ε_{zz} (%)	ε_{xx} (%)	ε_{yy} (%)	ε_{zz} (%)
MM	–	−17.022±0.094	−6.501±0.220	–	−16.575±0.057	−6.272±0.135	–	−16.711±0.082	−6.120±0.094
ME	29.672	−8.33 saturated	–	29.672	−8.33 saturated	–	29.672	−8.33 saturated	–
2D DIC	31.125	−17.491	–	29.981	−17.274	–	29.595	−17.101	–
3D DIC	31.538	−17.523	–	29.740	−17.212	–	29.352	−17.012	–
USG	32.350±0.160	−17.808±0.136	−6.609±0.274	30.320±0.131	−16.800±0.183	−6.221±0.112	30.443±0.137	−17.158±0.234	−6.338±0.194

MM micrometer, *EM* extensometer, *2D/3D DIC* mono-/stereovision digital image correlation and *USG* ultrasonic strain gauge. The EM row is put in gray because only 1 measurement was obtained at a fixed and different location, while the signal in the *y*-direction saturated

subsequent subsets is based on the zero-normalized sum of squared differences (ZNSSD) criterion. This algorithm compensates for illumination differences taking into account the offset and linear scale of light intensity providing a robust noise-proof performance. Sub-pixel correlation is performed by using bicubic polynomial gray level interpolation. The surface strain field is computed using the sub-pixel measured displacement field. A strain window containing 25× 25 discrete displacement data points is approximated using a bilinear polynomial. The Biot strain tensor is then computed using these estimated displacement terms. In the absence of material rotations, which may be assumed for the here presented results, the Biot tensor simply corresponds to the engineering strain [23].

The size of the subset window depends on the quality and granularity of the speckle pattern and defines the displacement spatial resolution. Strain spatial resolution can be controlled by the size of the strain window and the step size. Lowering the step size makes adjacent subsets to overlap, thus increasing the strain spatial resolution. A larger strain window yields higher precision and accuracy, however this is less advantageous for investigating heterogeneous deformations. Therefore, a compromise must be found between these different parameters. The correlation criteria and calculation parameters for the experimental DIC setups used in this study are listed in Table 2.

A visualization of the longitudinal and transverse strain field (3D DIC) for the DC06-10 sample is displayed in Fig. 6(b-c). The results clearly reveal the non-uniformity of the strain field, which was already indicated by the MM extracted strains. Both the 2D and 3D DIC extracted longitudinal and transverse strains are added to Table 1 for the three aforementioned locations L_1, L_2 and L_3. Differences between mono- and stereovision data can be attributed to out-of-plane displacements due to Poisson's contractions as well as to deviations from the planarity [19]. Comparison of the DIC data with the MM and ME data yields good correspondence, indicating the consistency of the determined strain values.

Finally, the results obtained with the developed ultrasonic strain gauge are discussed. Instead of externally applying a specific surface corrugation to the DC06 steel, which would obviously weaken the steel sheet, we simply exploit the deterministic surface roughness (see Fig. 2) left by the work rolls during manufacturing. This surface roughness is an imperfect but periodic structure which can be conceived as two overlapping 1D gratings (see Fig. 2). The H-UBPS of a virgin DC06 sample is shown in Fig. 7. The here shown H-UBPS experiments cover [−60°,60°] for the incident angle θ and [0°,180°] for the polar angle φ, with the angular resolution fixed at $\Delta\theta$= 0.05° respectively $\Delta\varphi$=0.5°.

Despite the low surface finishing quality, the presence of many defects in the surface periodicities as well as the limited corrugation depth, distinct diffraction peaks can be observed.

Table 2 Optical system and correlation parameters

	Monovision 2D DIC	Stereovision 3D DIC
Noise Camera 0	0.68 %	0.73 %
Noise Camera 1	–	0.97 %
Pre-Filtering	Gaussian 5	Gaussian 5
Subset	31	31
Step	5	5
Correlation criterion	ZNSSD[a]	ZNSSD
Shape function	Affine	Affine
Interpolation function	Bicubic polynomial	Bicubic Polynomial
Displacement		
Spatial resolution	31 pixels	31 pixels
In-plane resolution	0.00947 mm	0.00242 mm
Out-of-plane resolution	–	0.01433 mm
Strain		
Strain window	25	25
Smoothing method	Polynomial bilinear	Polynomial bilinear
Virtual strain gauge	121 pixels	121 pixels
Spatial resolution	151 pixels	151 pixels
Resolution	153 μs	167 μs

[a] Zero-normalized sum of squared differences

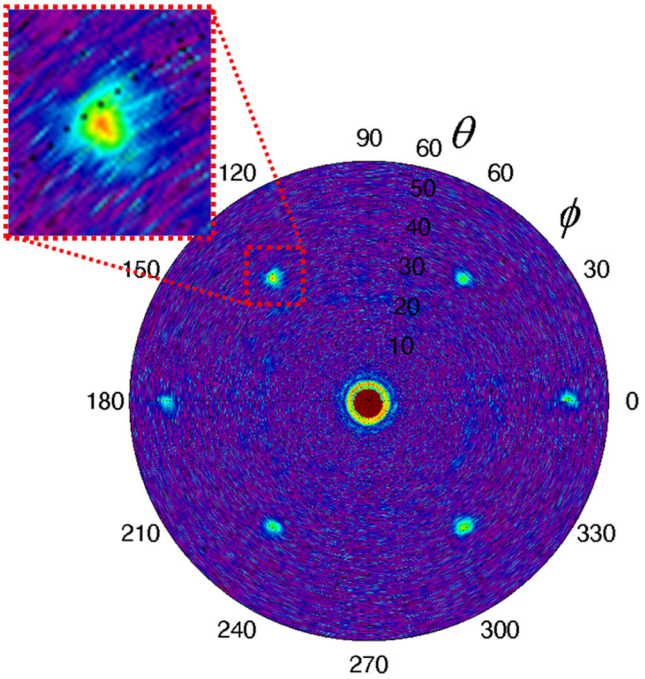

Fig. 7 H-UBPS recording at f=5 MHz for cold-rolled DC06 steel in virgin state

However, because the experimentally recorded peaks are smeared out in (ϕ,θ) -space due to the angular frequency content of the employed transducer, combined with the presence of experimental noise (see inset of Fig. 7), the extraction of the true spike locations becomes complicated. As such, the accuracy and reproducibility of the determined grating parameters, and in extension of the extracted strain field is jeopardized. Therefore, the experimental recording has been first convolved by a Gaussian kernel being representative for the spatial amplitude distribution of the employed ultrasonic wave. The surface parameters, extracted from the H-UBPS experiments of 7 different virgin DC06 samples, are listed in Table 3. It can be verified that the H-UBPS extracted parameters are within the range of the optically determined values (see Fig. 2(b)). More important, the robustness of both the H-UBPS methodology and the subsequent extraction procedure is well reflected in the small standard deviation. It is noted that the spatially bounded nature of the employed ultrasonic beam insonifies a local circular area with radius ~4 mm, and as such images a set of ~900 surface unit cells. This immediately explains the insensitivity of the H-UBPS methodology to random defects in the surface structure. As a matter of fact, some samples were slightly corroded when measured. Since every sheet of steel manufactured with the same set of work rolls has an identical surface texture, the extracted surface parameters listed in Table 3 are used as the reference parameters for the deterministic surface structure of the here considered cold-rolled DC06 steel.

The H-UBPS image of the strained DC06-10 sample (location 1) is shown in Fig. 8(a). One can clearly discern the positional shift of the diffraction peaks with respect to the H-UBPS results for the virgin sample. This is explicitly demonstrated in Fig. 8(b), which shows the extracted diffraction spots for both the virgin and the strained DC06-10 sample. Evaluation of the coordinate transformation of the diffraction peaks $(\phi^V,\theta^V)\rightarrow(\phi^S,\theta^S)$ according to the analysis presented in section IIA, then yields the local in-plane strain field components. Four H-UBPS experiments have been performed to each of the three spots from which the average value and the standard deviation is obtained. The results have been added to Table 1 (row USG). Good agreement is obtained with the in-plane normal strain field components obtained with the other techniques. The low standard deviation further indicates the reproducibility of the H-UBPS results for measuring in-plane strain components by exploiting changes in the residual surface roughness.

The determination of the out-of-plane strain field is done according to the scheme given in Section IIB. An ultrasonic pulse is emitted to the zone of interest at normal incidence (identifiable in the H-UBPS image), after which the reflected signal is recorded in a time window of 50 μs at 10-bit resolution (time grid of 1,024 points). To minimize edge effects at the borders of the recorded time signal, which result in spectral leakage in the FFT spectrum, the time signals have been windowed by means of a Tukey (tapered cosine) function [24], setting the ratio of the cosine-tapered section length to the entire window length equal to 0.25. Zero padding has been applied to the windowed signal, resulting in a FFT vector having an increased number of bins which are more closely spaced in frequency space. Obviously, zero padding does not add any information, but has the same effect as the application of a high-quality sinc-interpolation [25] to the original data. The fast Fourier transform is then applied to the zero-padded data. It was found that the true thickness resonance occurred at fd=3.19 MHz.mm, which is in close agreement with the numerically computed thickness resonance (fd= 3.11 MHz.mm), thus indicating the precision of the

Table 3 Obtained results for the surface texture of cold-rolled DC06 steel sheet: CCI corresponds to the optically measured parameters (see Fig. 2(b)), H-UBPS are the ultrasonically (at f=5 MHz) determined parameters

	Λ_1^V [μm]	Φ_1^V [°]	Λ_2^V [μm]	Φ_2^V [°]	Λ_{1+2}^V [μm]	Φ_{1+2}^V [°]
CCI	243±20.2	53	243±23.6	125	191±16	0
H-UBPS	233.9033±0.8533	53.0167±0.0816	233.8183±0.7765	127.9250±0.1369	193.7360±1.4119	0.96±0.1782

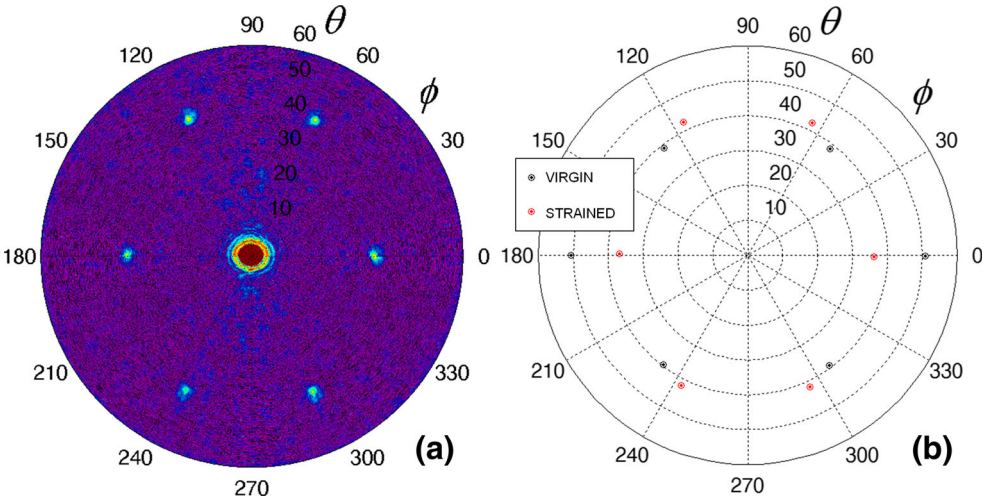

Fig. 8 H-UBPS recording at f= 5 MHz for the strained DC06-10 sample (**a**) and extracted diffraction peaks for the virgin DC06 sample (*black*) and the strained (*red*) DC06-10 sample (**b**)

considered material parameters. Note that the presence of a surface corrugation induces additional phenomena for normal incident waves [26, 27], though it is found that these effects do not interfere with the envisioned phenomenon, probably because of the very limited depth (~1.1 μm) of the here considered surface structure. The dip in reflected amplitude has been

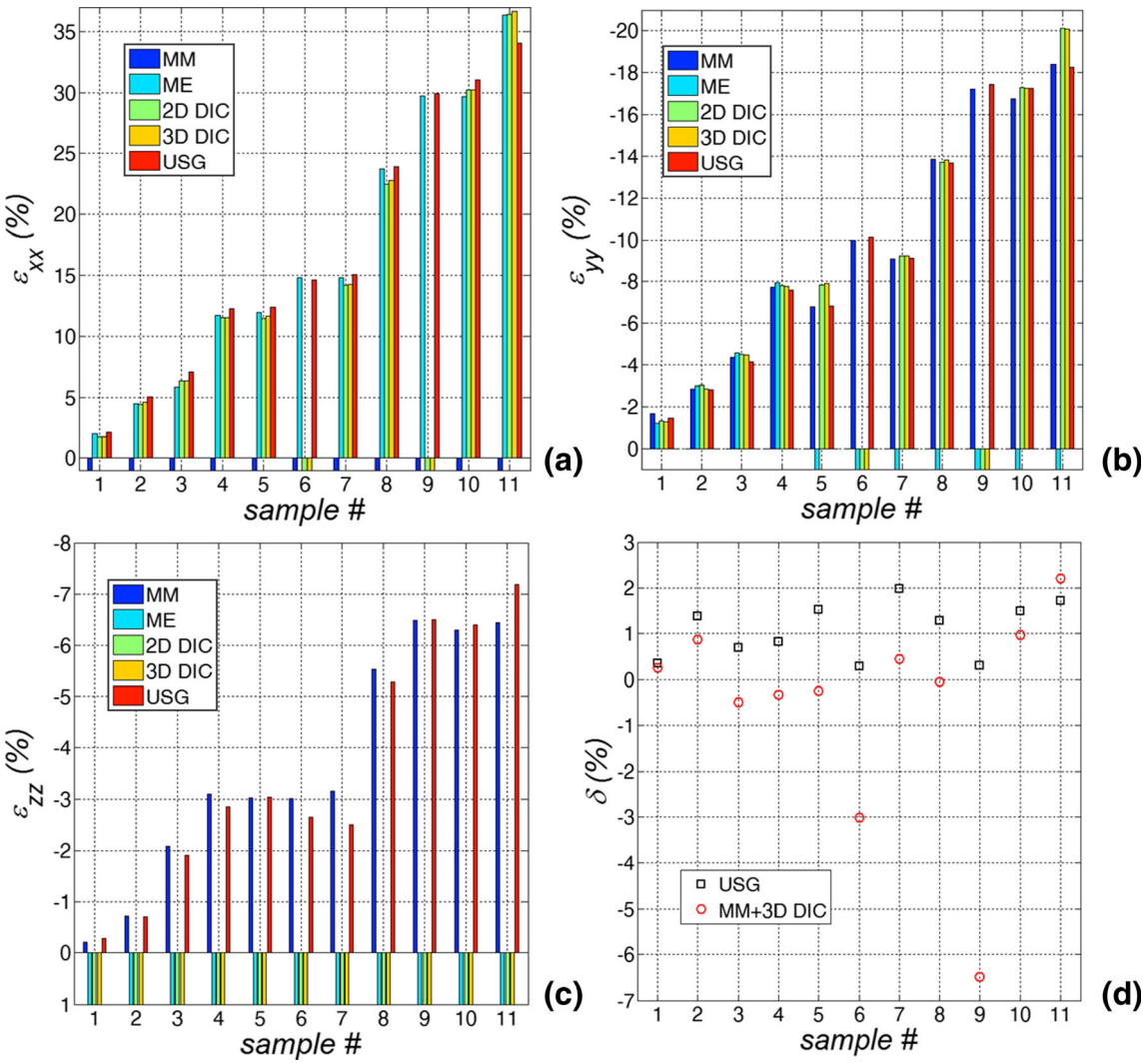

Fig. 9 Extracted strain values: longitudinal (**a**), transverse (**b**) and thickness (**c**) component. Error δ on the incompressibility hypothesis (**d**)

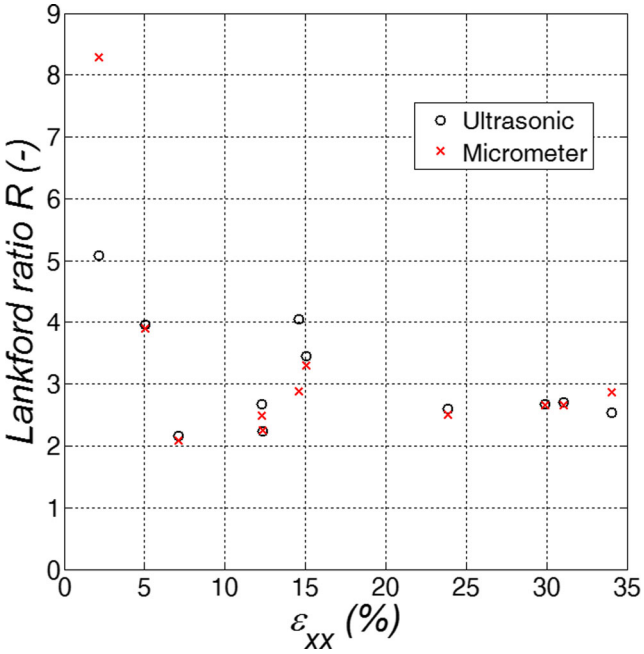

Fig. 10 Lankford ratio R transverse to the rolling direction as a function of applied longitudinal strain ε_{xx}: USG (*black* +) and MM (*red* x)

tracked as a function of frequency. Ten measurements have been performed at the different spots from which an average value and a standard deviation are obtained. The results are added to Table 1 (row USG). Unfortunately, neither the ME, nor the DIC technique can measure the out-of plane strain field component. Therefore, only comparison with the MM measurements can be done, yielding good agreement.

Several other plastically strained DC06 samples (all loaded transverse to the rolling direction) have been processed and analyzed in a similar way as done above for the DC06-10 sample. For brevity however, we only graphically display the strain values extracted by the different measurement techniques (see Fig. 9(a-c)). It has been found that several strain values were corrupted/missing because of (i) the insensitivity of a method for a certain strain field component, (ii) the limited range for strain amplitude in case of the transverse ME and (iii) occasional debonding of the speckle pattern for the mono- and stereovision DIC. For clarity, these corrupted/missing values are set at fictitious values of-1 % for the longitudinal strain component, and at +1 % for the transverse and the thickness strain component. In fact, the USG is the only method which successfully determined both the in-plane and the out-of-plane strain components for all the tested samples without any difficulty encountered. It can be verified in Fig. 9(a-c) that the USG extracted strain values show good correspondence with the other sets of partial strain data, and this over the full range of considered plastic strains.

The incompressibility hypothesis, which states that volume remains constant upon plastically straining a sample, provides another check for the accuracy and validity of the extracted strain field components. This is graphically presented for the USG data set in Fig. 9(d) (black squares). It can be readily verified that the error δ (in %) on the incompressibility hypothesis is within narrow bounds. Unfortunately, this hypothesis cannot be checked for the strain values obtained by the other strain gauge techniques as none of them provide the three needed normal strain field components ε_{xx}, ε_{yy} and ε_{zz}. However, if one would consider the combination of the 3D DIC in-plane components ε_{xx} and ε_{yy} and the MM out-of-plane component ε_{zz}, a hybrid measure of the incompressibility hypothesis (see red circles in Fig. 9(d)) is obtained. Except for the two outliers (corrupted DIC data), it can be observed that the error δ has the same order of magnitude as was found for the USG data set.

Knowledge of the three normal plastic strain components further allows the determination of the Lankford coefficient R_{ij} which is a measure of strain-anisotropy in the plastic regime. For a uniaxial test on a rectangular sheet specimen the Lankford coefficient R_{ij} is defined by [28]

$$R_{ij} = -\frac{\varepsilon_{jj}^{PL}}{\varepsilon_{ii}^{PL}} \tag{10}$$

with ε_{ii}^{PL} and ε_{jj}^{PL} the plastic strain in the width, respectively thickness direction of the sample.

As tensile tests have been performed at various strain levels, the Lankford coefficient can be evaluated as a function of applied longitudinal strain. In order to backup the USG extracted Lankford coefficients, we have also determined the Lankford ratios on the basis of the MM measurements. Strictly speaking, the latter is impossible as the MM does not provide a measure for the longitudinal strain component. However, as there is no alternative we set the longitudinal strain component equal to the USG extracted value. The obtained results are graphically displayed in Fig. 10. Except for the Lankford parameter at $\varepsilon_{xx}\approx 2$ % (division of small numbers), good agreement is obtained between both sets of data. The results indicate a dependency of the Lankford parameter on the applied longitudinal strain level, which is consistent with recent observations in literature [28]. However, contrary to literature we extracted the Lankford ratios by direct measurement of all the required normal strain field components without further assumptions or restrictions. According to [28], a Lankford ratio of $R\sim 2.5$ (loading transverse to the rolling direction) should be obtained at large longitudinal strain levels, which agrees well with the presented data in Fig. 10. Due to the rolling process, the plastic anisotropy is dependent on the in-plane orientation. Therefore other Lankford ratios will be obtained for DC06 specimen cut at a different direction [28]. As such a yield surface can be constructed in order to capture the anisotropic plastic behavior of steel sheet. Though, the latter is beyond the scope of this study.

Conclusions

A novel ultrasonic strain gauge method has been introduced for the local measurement of a 3D strain field. The in-plane strain field is measured by exploiting the interaction of oblique incident ultrasonic waves with a deterministic surface roughness, while the out-of-plane component is extracted by tracing changes in the stimulation condition of a thickness resonance. The method has been applied to cold-rolled DC06 steel samples onto which skin passing of the work rolls was applied during rolling. Several DC06 samples have been loaded by means of a tensile machine to induce various plastic strain fields ranging from ~2 % up to ~35 %. The ultrasonic strain measurements have been validated with several conventional strain gauge techniques: good correspondence with the other sets of (partial) strain data is obtained, and this for all considered strain levels. In addition, the capability of the ultrasonic strain gauge has been demonstrated by extracting the Lankford ratios transverse to the rolling direction for the DC06 steel as a function of applied longitudinal strain.

The here presented ultrasonic strain gauge locally measures all normal strain field components in an absolute way using a single-sided non-contact approach without the need of sample preparation, and for which alignment is of minor concern. As such, it has great appeal for industrial applications, especially when the occasional assessment of a strain field over long periods is required because the method provides an absolute strain measure whenever a measurement is performed.

It would be beneficial to construct a miniaturized device on the basis of advanced phased matrix (2D array) technology in order to (i) increase accuracy, (ii) simplify the experimental setup and (iii) reduce the experimental time drastically. Such a hand-held device would make it possible to scan a complete surface within a reasonable time (in the order of seconds), and would meet in-field requirements thus expanding the applicability of the ultrasonic strain gauge to the measurement of elastic strain fields. Efforts in this direction are currently going on in our research lab.

Acknowledgments Mathias Kersemans acknowledges funding of the FWO-Vlaanderen through grant G012010N.

References

1. Ostby E, Jayadevan KR, Thaulow C (2005) Fracture response of pipelines subject to large plastic deformation under bending. Int J Press Vessel Pip 82:201–215
2. Jayadevan KR, Ostby E, Thaulow C (2004) Fracture response of pipelines subjected to large plastic deformation under tension. Int J Press Vessel Pip 81:771–783
3. Mohr W (2003) Strain-Based design of Pipelines. Report Project No. 45892GTH, U.S. Department of Interior, Minerals Management Service and U.S. Department of Transportation Research and Special Programs Administration
4. Arshak A, Arshak K, Morris D, Korostynska O, Jafer E (2005) Investigation of TiO2 thick film capacitors for use as strain gauge sensors. Sensors Actuators A Phys 122:242–249
5. Herrmann J, Muller KH, Reda T, Baxter GR, Raguse B, de Groot G, Chai R, Roberts M, Wieczorek L (2007) Nanoparticle films as sensitive strain gauges. Applied Physics Letters 91
6. Betz DC, Thursby G, Culshaw B, Staszewski WJ (2006) Advanced layout of a fiber Bragg grating strain gauge rosette. J Lightwave Technol 24:1019–1026
7. Viotti MR, Albertazzi AG, Kapp W (2008) Experimental comparison between a portable DSPI device with diffractive optical element and a hole drilling strain gage combined system. Opt Lasers Eng 46:835–841
8. Zhao B, Xie HM, Asundi A (2001) Optical strain sensor using median density grating foil: Rivaling the electric strain gauge. Rev Sci Instrum 72:1554–1558
9. Cofaru C, Philips W, Van Paepegem W (2012) A three-frame digital image correlation (DIC) method for the measurement of small displacements and strains. Measurement Science & Technology 23
10. Pinto JMT, Touchard F, Castagnet S, Nadot-Martin C, Mellier D (2013) DIC Strain Measurements at the Micro-Scale in a Semi-Crystalline Polymer. Exp Mech 53:1311–1321
11. Bragg WL (1913) The diffraction of short electromagnetic waves by a crystal. Proc Cambridge Phil Soc 17:43–57
12. Kersemans M, Van Paepegem W, Van Den Abeele K, Pyl L, Zastavnik F, Sol H, Degrieck J (2014) Ultrasonic Characterization of Subsurface 2D Corrugation. J Nondestruct Eval 33(3):438–442. doi:10.1007/s10921-014-0239-7
13. Kersemans M, Martens A, Lammens N, Van Den Abeele K, Degrieck J, Zastavnik F, Pyl L, Sol H, Van Paepegem W (2014) Identification of the elastic properties of isotropic and orthotropic thin-plate materials with the pulsed ultrasonic polar scan. Exp Mech 54(6):1121–1132. doi:10.1007/s11340-014-9861-7
14. ArcelorMittal(SouthAfrica), Data sheet: B3.1 Cold Rolled Steel Sheet for Drawing and Forming EN 10130 DC01-DC06, in, 2010.
15. Scheers J, De Mare C, Iron, S.O.C. Steel, The use of 'fine-deterministic' steel sheet textures to improve the drawability and paint quality of high strength body panels, in, 40th Mechanical Working and Steel Processing Conference Proceedings, Vol Xxxvi, 1998, pp. 93–99.
16. ASTM, E8/E8M-08. Standard Test Methods for Tension Testing of Metallic Materials
17. Sutton MA, Orteu J-J, Schreier HW (2009) Image correlation for shape, motion and deformation measurements. Springer, New York
18. MatchID_software, <http://www.matchid.org/>
19. Sutton MA, Yan JH, Tiwari V, Schreier HW, Orteu JJ (2008) The effect of out-of-plane motion on 2D and 3D digital image correlation measurements. Opt Lasers Eng 46:746–757
20. Kersemans M, Van Paepegem W, Van Den Abeele K, Pyl L, Zastavnik F, Sol H, Degrieck J (2014) Pitfalls in the experimental recording of ultrasonic (backscatter) polar scans for material characterization. Ultrasonics 54(6):1509–1521. doi:10.1016/j.ultras.2014.04.013
21. Kersemans M, Martens A, Van Den Abeele K, Degrieck J, Pyl L, Zastavnik F, Sol H, Van Paepegem W (2014) Detection and localization of delaminations in thin carbon fiber reinforced composites with the ultrasonic polar scan. J Nondestruct Eval doi:10.1007/s10921-014-0249-5
22. Matar OB, Gasmi N, Zhou H, Goueygou M, Talbi A (2013) Legendre and Laguerre polynomial approach for modeling of wave propagation in layered magneto-electro-elastic media. J Acoust Soc Am 133:1415–1424
23. Bazant ZPA (1996) M.D., Y. Xiang, Finite Strain Analysis of Deformations of Quasibrittle Material during Missile Impact and Penetration. In: Clifton RJ, Espinosa HD (eds) Advances in Failure Mechanics in Brittle Materials. The American Society of Mechanical Engineers, Atlanta, Georgia

24. Tukey JW (1968) An introduction to the calculations of numerical spectrum analysis. Wiley, New York
25. Unser M (2000) Sampling - 50 years after Shannon. Proc IEEE 88: 569–587
26. Mampaert K, Nagy PB, Leroy O, Adler L, Jungman A, Quentin G (1989) On the origin of the anomalies in the reflected ultrasonic spectra from periodic surfaces. J Acoust Soc Am 86:429–431
27. Jungman A, Adler L, Quentin G (1982) Ultrasonic anomalies in the spectrum of acoustic-waves diffracted by periodic interfaces. J Appl Phys 53:4673–4680
28. Safaei M, Constitutive modelling of anisotropic sheet metals based on a non-associated flow rule. Ghent University, Faculty of engineering sciences and architecture (Ghent), PhD thesis (2013) 246